Boundary-Layer Meteorology (2006) 119: 375–395
DOI 10.1007/s10546-005-9015-7

CORRECTIONS TO INERTIAL-RANGE POWER SPECTRA MEASURED BY CSAT3 AND SOLENT SONIC ANEMOMETERS, 1. PATH-AVERAGING ERRORS

T. W. HORST* and S. P. ONCLEY
National Center for Atmospheric Research, Atmospheric Technology Division, P.O. Box 3000, Boulder, CO, 80307-3000, U.S.A.

(Received in final form 1 August 2005 / Published online: 10 May 2006)

Abstract. Sonic anemometer path-averaging errors are determined for measurements of inertial-range velocity and temperature power spectra as a function of $k_1 p$, where k_1 is the streamwise wavenumber and p is the sonic path length. The attenuation of vertical velocity spectra is found to be quite similar for the CSAT3 and Solent anemometers and to be insensitive to wind direction. The attenuation of the horizontal wind component spectra is noticeably greater for the Solent sonics than for the CSAT3, but those for the CSAT3 have a greater dependence on wind direction. The attenuation of sonic temperature spectra is also found to be quite similar for the CSAT3 and Solent R3 sonics and to be insensitive to wind direction, while that of the Solent R2 is less than that of the other two sonics and has a minor dependence on wind direction.

Keywords: Path-average error, Sonic anemometer, Spectral corrections.

1. Introduction

Measurement of atmospheric surface-layer turbulence at fine scales has been a subject of continuing interest in recent years. Studies of turbulence in stable conditions (Howell and Sun, 1999), shallow drainage flows (Mahrt et al., 2001), and measurement of dissipation in the inertial range (Fairall et al., 2003) all require data at spatial scales on the order of 0.1m or smaller. However, the most robust instruments for measuring atmospheric turbulence – sonic anemometers – are forced by current transducer technology and concerns about flow distortion to have dimensions on the order of 0.1m or larger. Sonic anemometers determine the vector wind components and sound virtual temperature by measuring the transit times of sound pulses traveling in opposite directions along each of three acoustic paths. As a consequence, the wind and temperature measurements are spatially

* E-mail: horst@ucar.edu

TABLE I
Design parameters of UW-Geometry sonics.

Sonic	ϕ (degrees)	path length (m)	speed of sound (Number of paths)
UW	60	0.20	3
K–D TR–61B	45	0.20	1
Solent R2	45	0.15	1
Solent R3	45	0.15	3
CSAT3	60	0.115	3

averaged along the length of the measurement paths, thus attenuating spatial variations that have wavelengths on the order of and shorter than the path length. Nevertheless, these anemometers may be used for these applications if their response to small scales can be modelled. Here, we calculate the effect of sonic anemometer path averaging for measurement of inertial-range power spectra by two current commercial sonic anemometer designs.

Kaimal et al. (1968) determined the attenuation of velocity power spectra in the inertial range for a three-dimensional sonic anemometer with a path geometry consisting of a single vertical path combined with two horizontal paths separated by an angle of 120°. Horst (1973) extended their analysis to account for additional spatial separations of the sonic paths found in the Kaijo–Denki TR-61A sonic anemometer. At the same time, Silverman (1968) derived the attenuation of scalar power spectra due to spatial averaging along a single path. Since then, several sonic anemometer designs have adopted the path geometry introduced by Joost Businger and Steve Oncley at the University of Washington. The UW sonic anemometer (Zhang et al., 1986) features three 0.2 m paths that intersect at a common centre point and are oriented at an angle $\phi = 60°$ above the horizontal (see, for example, Figure 1). The projections of the three paths onto the horizontal plane are located at 120° intervals. The goal of the UW geometry is to remove the sonic paths from the horizontal plane in order to minimize the "transducer shadow error", that is, the velocity deficit that occurs when the wakes of the transducers intrude into the measurement path (Wyngaard and Zhang, 1985). Around the time that the UW sonic was developed, Kaijo–Denki independently developed and introduced their model TR-61B with a similar geometry, but with $\phi = 45°$. The more recent Solent R2 and R3 sonic anemometers use the Kaijo–Denki path geometry, but with 0.15 m path lengths, and the new Campbell Scientific CSAT3 uses the original UW geometry with 0.115 m paths. The design parameters of sonics with UW path geometries are listed in Table I.

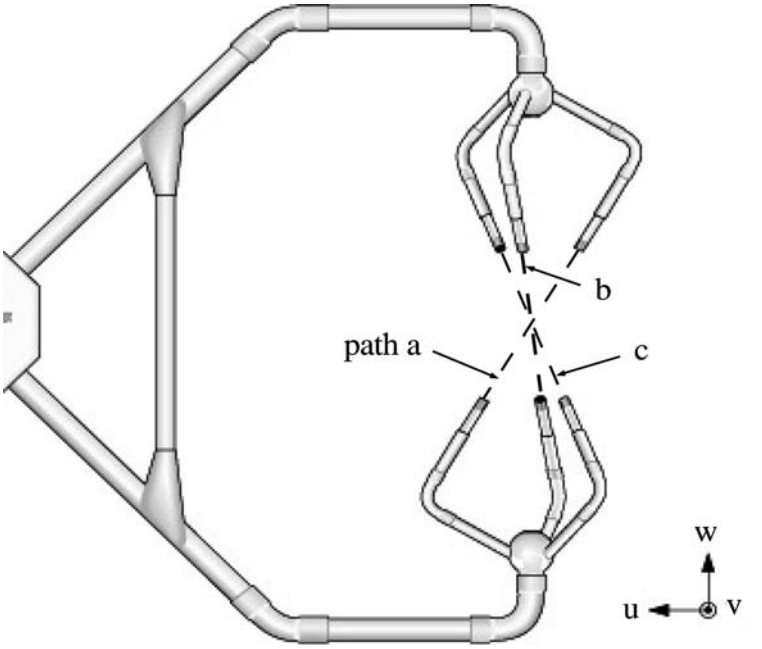

Figure 1. Path geometry of the CSAT3 sonic anemometer and the orthogonal wind components in instrument coordinates. Drawing courtesy T. Davidson and E. Swiatek, Campbell Scientific, Inc.

This paper applies the path-average analysis of Kaimal et al. (1968, hereafter KWH) and Silverman (1968) to the generic UW sonic path geometry. In the concluding section we add to this the effects of aliasing and oversampling (Appendix C) and show how to combine these with path-averaging to correct measured power spectra in the inertial range.

2. The Basics

The wind velocity **u** averaged along a single sonic path of length p is

$$\tilde{\mathbf{u}}(\mathbf{x}_o, \mathbf{p}) = \frac{1}{p}\int_{-p/2}^{p/2} \mathbf{u}(\mathbf{x}_o + \mathbf{s})\, ds. \tag{1}$$

Here $\mathbf{u}(\mathbf{x})$ is the wind velocity vector at point $\mathbf{x}$, $\mathbf{x}_o$ is the centre point of the sonic path, and the variable of integration $\mathbf{s}$ is parallel to the sonic path $\mathbf{p}$. By representing the velocity field in terms of its Fourier components, KWH showed that the ratio of the path-averaged to the true one-dimensional, streamwise power spectrum is

$$H_i(k_1, \mathbf{p}) = \frac{\iint_{-\infty}^{\infty} \mathrm{sinc}^2(\mathbf{k}\cdot\mathbf{p}/2)\, \Phi_{ii}(\mathbf{k})\, dk_2\, dk_3}{\iint_{-\infty}^{\infty} \Phi_{ii}(\mathbf{k})\, dk_2\, dk_3}, \tag{2}$$

where $\mathrm{sinc}(x) \equiv \sin(x)/x$, $\mathbf{k}$ is a wavenumber vector with components k_1 in the streamwise direction, k_2 in the crosswind direction and k_3 in the vertical direction, and $\Phi_{ii}(\mathbf{k})$ is the spectral density for velocity component u_i. KWH refer to H_i as a spectral transfer function. Note that for the special case when the path $\mathbf{p}$ lies in the streamwise direction,

$$H_1(k_1 p) = \mathrm{sinc}^2(k_1 p/2). \tag{3}$$

Assuming isotropy and $\mathbf{k}$ in the inertial range, the spectral density tensor for velocity is

$$\Phi_{ij}(\mathbf{k}) = \frac{C_u \epsilon^{2/3} k^{-5/3}}{4\pi k^4}(k^2\delta_{ij} - k_i k_j), \tag{4}$$

where k is the magnitude of $\mathbf{k}$, ϵ is the rate of turbulent energy dissipation, and C_u is the Kolmogorov constant for velocity (Pope, 2000). Sonic anemometers also measure the speed of sound, from which can be calculated the sound virtual temperature T_s. Equations (1) and (2) also apply to path-averaged measurements of sonic temperature, using instead

$$\Phi_{T_s}(k) = \frac{C_T N_{T_s} \epsilon^{-1/3} k^{-5/3}}{2\pi k^2}, \tag{5}$$

(Tennekes and Lumley, 1972) where N_{T_s} is the rate of dissipation of sonic temperature variance and C_T is the Kolmogorov constant for temperature. The denominator of Equation (2) is the one-dimensional spectral density and can be evaluated analytically for the three-dimensional, inertial-range spectral densities (4) and (5). For velocity,

$$S_i(k_1) = \iint_{-\infty}^{\infty} \Phi_{ii}(\mathbf{k})\, dk_2\, dk_3 = \begin{cases} \frac{9}{55} C_u \epsilon^{2/3} k_1^{-5/3}, & i = 1 \\ \frac{12}{55} C_u \epsilon^{2/3} k_1^{-5/3}, & i = 2, 3 \end{cases}, \tag{6}$$

and for sonic temperature,

$$S_{T_s}(k_1) = \iint_{-\infty}^{\infty} \Phi_{T_s}(\mathbf{k})\, dk_2\, dk_3 = \frac{3}{5} C_T N_{T_s} \epsilon^{-1/3} k_1^{-5/3}. \tag{7}$$

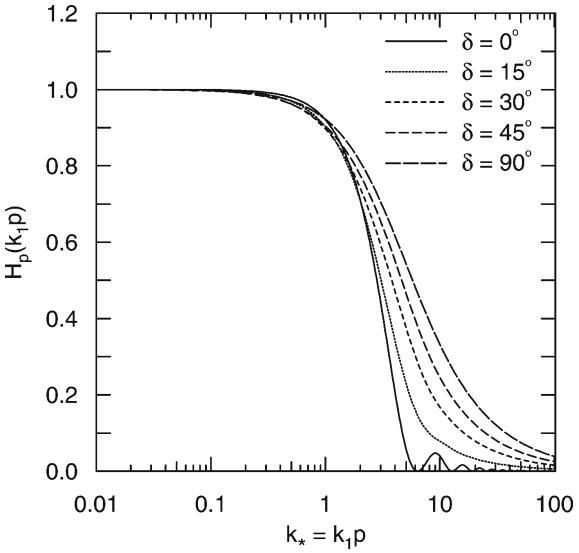

Figure 2. Transfer functions for measurement of velocity spectra by a single sonic path.

3. Spectral Transfer Functions for Velocity

For the special case of velocity measurement along a single path, one of the integrals in the numerator of (2) can be determined analytically,

$$H_p(k_1 p, \delta) = \frac{11\,\Gamma(4/3)k_1^{5/3}}{2\sqrt{\pi}\,\Gamma(5/6)(4-\cos^2\delta)} \int_{-\infty}^{\infty} \frac{\left(k_1^2 + k'^2 - (8/11)(k_1\cos\delta + k'\sin\delta)^2\right)}{(k_1^2+k'^2)^{7/3}} \times \operatorname{sinc}^2(k_1 p\cos\delta/2 + k' p\sin\delta/2)\,dk', \tag{8}$$

where δ is the angle between the sonic path and the streamwise wind direction. Figure 2 shows H_p as a function of $k_1 p$ for $0 \le \delta \le 90^\circ$. $H_p(\delta = 0)$ reduces to Equation (3) and $H_p(\delta = 90^\circ)$ is the transfer function for measurement of the vertical velocity by a vertical path. The transfer functions for these two limits were shown previously in KWH. Note the strong dependence on δ at small values of δ and the weaker dependence as δ approaches 90°, possibly due to the $k'\sin\delta$ terms in (8). The analytical result of Equation (8) is useful for testing the numerical integration methods required to evaluate Equation (2) for the general case of the UW sonic geometry.

The UW sonic geometry, shown in Figure 1, uses all three paths to measure the orthogonal wind components. We follow the convention of the CSAT3 sonic and denote the three paths as *a*, *b*, *c* (arranged in

clockwise order of the upper transducers when viewed from above). The wind components in an orthogonal coordinate system fixed to the sonic anemometer are

$$u = \frac{-2u_a + u_b + u_c}{3\cos\phi}, \tag{9a}$$

$$v = \frac{u_b - u_c}{\sqrt{3}\cos\phi}, \tag{9b}$$

$$w = \frac{u_a + u_b + u_c}{3\sin\phi}. \tag{9c}$$

where u_a, u_b and u_c are the wind components parallel to the three paths, assumed positive from the lower to the upper transducer, and ϕ is the angle of the paths above the horizontal. In these instrument coordinates, the horizontal wind component u is aligned with the vertical plane containing path a. The inverse coordinate transformation is

$$u_a = -u\cos\phi + w\sin\phi, \tag{10a}$$

$$u_b = \frac{u + \sqrt{3}v}{2}\cos\phi + w\sin\phi, \tag{10b}$$

$$u_c = \frac{u - \sqrt{3}v}{2}\cos\phi + w\sin\phi. \tag{10c}$$

Finally, the wind components in an orthogonal coordinate system aligned with the streamwise wind direction are

$$u_1 = u\cos\theta + v\sin\theta, \tag{11a}$$

$$u_2 = -u\sin\theta + v\cos\theta, \tag{11b}$$

$$u_3 = w, \tag{11c}$$

where u_1 is in the streamwise direction and θ is the angle between u_1 and u. Note that Equations (11) assume that the sonic is properly aligned in the vertical direction.

Following the analysis of KWH, we then find

$$\begin{aligned} u_1^m = {} & \tfrac{2}{3}[\tilde{u}_1^a\cos^2\theta + \tilde{u}_1^b\cos^2(\theta - \pi/3) + \tilde{u}_1^c\cos^2(\theta + \pi/3)] \\ & -\tfrac{1}{3}[\tilde{u}_2^a\sin 2\theta - \tilde{u}_2^b\sin(2\theta + \pi/3) - \tilde{u}_2^c\sin(2\theta - \pi/3)] \\ & -\frac{2\tan\phi}{3}[\tilde{u}_3^a\cos\theta - \tilde{u}_3^b\cos(\theta - \pi/3) - \tilde{u}_3^c\cos(\theta + \pi/3)], \end{aligned} \tag{12}$$

$$u_2^m = -\tfrac{1}{3}[\tilde{u}_1^a \sin 2\theta - \tilde{u}_1^b \sin(2\theta + \pi/3) - \tilde{u}_1^c \sin(2\theta - \pi/3)]$$
$$+\tfrac{2}{3}[\tilde{u}_2^a \sin^2\theta + \tilde{u}_2^b \sin^2(\theta - \pi/3) + \tilde{u}_2^c \sin^2(\theta + \pi/3)]$$
$$+\frac{2\tan\phi}{3}[\tilde{u}_3^a \sin\theta - \tilde{u}_3^b \sin(\theta - \pi/3) - \tilde{u}_3^c \sin(\theta + \pi/3)], \tag{13}$$

$$u_3^m = -\frac{\cot\phi}{3}[\tilde{u}_1^a \cos\theta - \tilde{u}_1^b \cos(\theta - \pi/3) - \tilde{u}_1^c \cos(\theta + \pi/3)]$$
$$+\frac{\cot\phi}{3}[\tilde{u}_2^a \sin\theta - \tilde{u}_2^b \sin(\theta - \pi/3) - \tilde{u}_2^c \sin(\theta + \pi/3)]$$
$$+\frac{1}{3}[\tilde{u}_3^a + \tilde{u}_3^b + \tilde{u}_3^c], \tag{14}$$

where u_j^m are the orthogonal velocity components in a streamwise coordinate system, computed from measurements along the three paths, and the j component of velocity averaged along path α is

$$\tilde{u}_j^\alpha(\mathbf{x}, \mathbf{p}_\alpha) = \frac{1}{p}\int_{-p/2}^{p/2} u_j(\mathbf{x}_\alpha + \mathbf{s}_\alpha)\, ds, \tag{15}$$

where $j = 1$, 2 or 3 and $\alpha = a$, b or c.

In order to determine the attenuation in wavenumber space, KWH and Silverman (1968) then introduce Fourier–Stieltjes representations,

$$u_j^m(\mathbf{x}) = \int_{-\infty}^{\infty} e^{i\mathbf{k}\cdot\mathbf{x}}\, dU_j^m(\mathbf{k}) \tag{16}$$

and

$$\tilde{u}_j^\alpha(\mathbf{x}, \mathbf{p}_\alpha) = \int_{-\infty}^{\infty} e^{i\mathbf{k}\cdot\mathbf{x}} \operatorname{sinc}(\mathbf{k}\cdot\mathbf{p}_\alpha/2)\, dU_j(\mathbf{k}), \tag{17}$$

where the $U_j(\mathbf{k}, t)$ are random functions with orthogonal increments

$$\overline{dU_i(\mathbf{k}) dU_j^*(\mathbf{k}')} = \begin{cases} 0, & \mathbf{k}' \neq \mathbf{k} \\ \Phi_{ij}(\mathbf{k})\, d\mathbf{k}, & \mathbf{k}' = \mathbf{k} \end{cases} \tag{18}$$

and an asterisk denotes a complex conjugate. Substitution of Equations (16–17) into Equations (12–14) gives

$$dU_j^m = C_{j1} dU_1 + C_{j2} dU_2 + C_{j3} dU_3, \tag{19}$$

where

$$
\begin{aligned}
C_{11} &= \tfrac{2}{3}\left[\cos^2\theta\,\mathrm{sinc}\,(\mathbf{k}\cdot\mathbf{p}_a/2) + \cos^2(\theta-\pi/3)\,\mathrm{sinc}\,(\mathbf{k}\cdot\mathbf{p}_b/2)\right.\\
&\qquad \left. + \cos^2(\theta+\pi/3)\,\mathrm{sinc}\,(\mathbf{k}\cdot\mathbf{p}_c/2)\right],\\
C_{12} &= -\tfrac{1}{3}\left[\sin 2\theta\,\mathrm{sinc}\,(\mathbf{k}\cdot\mathbf{p}_a/2) - \sin(2\theta+\pi/3)\,\mathrm{sinc}\,(\mathbf{k}\cdot\mathbf{p}_b/2)\right.\\
&\qquad \left. - \sin(2\theta-\pi/3)\,\mathrm{sinc}\,(\mathbf{k}\cdot\mathbf{p}_c/2)\right],\\
C_{13} &= -\frac{2\tan\phi}{3}\left[\cos\theta\,\mathrm{sinc}\,(\mathbf{k}\cdot\mathbf{p}_a/2) - \cos(\theta-\pi/3)\,\mathrm{sinc}\,(\mathbf{k}\cdot\mathbf{p}_b/2)\right.\\
&\qquad \left. - \cos(\theta+\pi/3)\,\mathrm{sinc}\,(\mathbf{k}\cdot\mathbf{p}_c/2)\right],\\
C_{21} &= C_{12},\\
C_{22} &= \tfrac{2}{3}\left[\sin^2\theta\,\mathrm{sinc}\,(\mathbf{k}\cdot\mathbf{p}_a/2) + \sin^2(\theta-\pi/3)\,\mathrm{sinc}\,(\mathbf{k}\cdot\mathbf{p}_b/2)\right.\\
&\qquad \left. + \sin^2(\theta+\pi/3)\,\mathrm{sinc}\,(\mathbf{k}\cdot\mathbf{p}_c/2)\right],\\
C_{23} &= \frac{2\tan\phi}{3}\left[\sin\theta\,\mathrm{sinc}\,(\mathbf{k}\cdot\mathbf{p}_a/2) - \sin(\theta-\pi/3)\,\mathrm{sinc}\,(\mathbf{k}\cdot\mathbf{p}_b/2)\right.\\
&\qquad \left. - \sin(\theta+\pi/3)\,\mathrm{sinc}\,(\mathbf{k}\cdot\mathbf{p}_c/2)\right],\\
C_{31} &= \frac{\cot^2\phi}{2}\,C_{13},\\
C_{32} &= \frac{\cot^2\phi}{2}\,C_{23},\\
C_{33} &= \tfrac{1}{3}\left[\mathrm{sinc}\,(\mathbf{k}\cdot\mathbf{p}_a/2) + \mathrm{sinc}\,(\mathbf{k}\cdot\mathbf{p}_b/2) + \mathrm{sinc}\,(\mathbf{k}\cdot\mathbf{p}_c/2)\right].
\end{aligned}
\tag{20}
$$

Finally,

$$
\Phi_{ii}^m = \overline{dU_i^m(\mathbf{k})[dU_i^m]^*(\mathbf{k})} = C_{ij}C_{il}\,\Phi_{jl}(\mathbf{k}),
\tag{21}
$$

where the summation convention applies to the repeated subscripts j and l, and

$$
H_i(k_1,\mathbf{p}) = \frac{\iint_{-\infty}^{\infty}\Phi_{ii}^m(\mathbf{k})\,dk_2\,dk_3}{\iint_{-\infty}^{\infty}\Phi_{ii}(\mathbf{k})\,dk_2\,dk_3} = \frac{\iint_{-\infty}^{\infty}C_{ij}C_{il}\,\Phi_{jl}(\mathbf{k})\,dk_2\,dk_3}{\iint_{-\infty}^{\infty}\Phi_{ii}(\mathbf{k})\,dk_2\,dk_3}.
\tag{22}
$$

See Appendix A for an alternate expression of C_{ij} that may be more amendable to coding for computer calculation, particularly when it is necessary to correct for sonic tilt.

The numerator of Equation (22) has been calculated numerically, using the extended trapezoidal rule (Press et al., 1992). Since the integrand is non-negligible over several decades of k_2 and k_3, the numerical integration has been calculated logarithmically over N decades in each of the four quadrants, e.g. $dk_2 = k_2\,d\ln k_2$, $k_0 \le k_2 \le 10^N k_0$. Accuracy of H_i to better

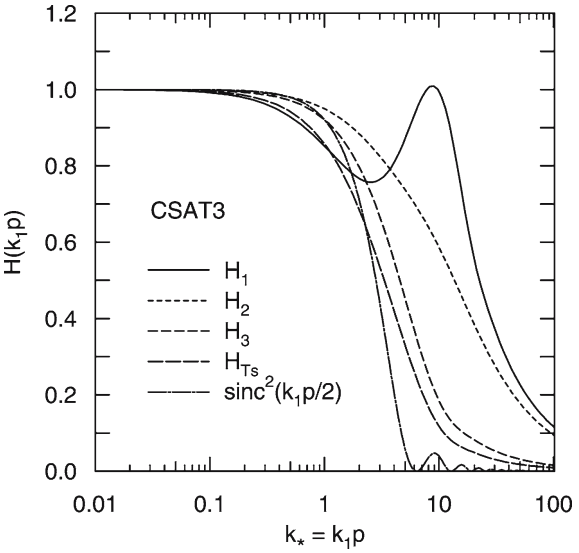

Figure 3. Transfer functions for measurement of velocity and temperature spectra by the CSAT3 sonic anemometer, $\theta = 0$.

than 0.01 is found for $k_0 = k_1 10^{-(3/4+N/2)}$, $N \geq 5$, and $S \geq 5$ integration steps per decade, i.e. $\Delta \ln k_2 = \ln(10)/S$. Results for calculations using $N = 7$ and $S \geq 10$ are tabulated in Appendix B.

Figures 3 and 4 show the transfer functions H_i for measurements of S_i by CSAT3 and Solent R3 (and R2) sonic anemometers. Both of these figures are for a wind direction parallel to the vertical plane containing one of the measurement paths, $\theta = 0$. Also shown for reference is the transfer function for the special case of measurement along a path parallel to the streamwise wind direction, Equation (3).

The transfer functions for the streamwise wind component decrease with increasing $k_* \equiv k_1 p$ at small values of the abscissa, but increase again at large values of k_*. The increase is more pronounced for the CSAT3 than for the Solent sonics, with the CSAT3 having a secondary peak at $k_* \approx 9$ versus a 'bump' for the Solent at $k_* \approx 7$. KWH observed this same behaviour for a sonic that has a geometry with two paths in the horizontal plane oriented at 120° with respect to each other but also with their centres separated by a distance $d/p = 0.6$. For that geometry, the secondary peak occurs at $k_* \approx 3$, but with $d/p = 0$, as for the UW geometry, KWH find a peak near $k_* = 10$. KWH attributed this behaviour to the spatial decorrelation between wind measurements along the separate paths and to the 4/3 ratio between the spectra of the transverse wind components, S_{22} and S_{33}, and the spectrum of the streamwise wind component S_{11}, see Equation (6). As a consequence, the contamination of the streamwise wind component

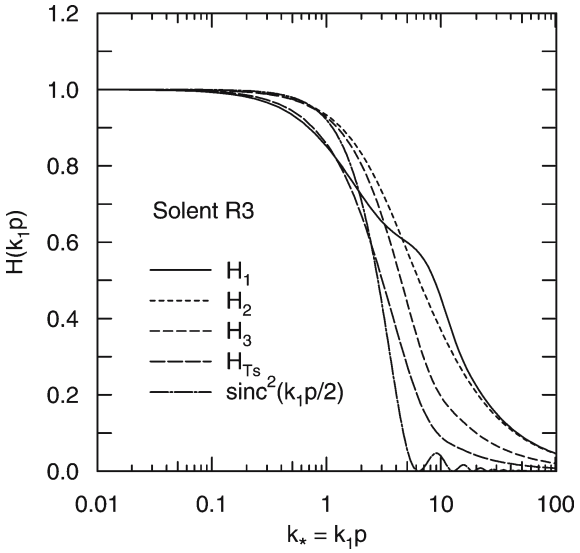

Figure 4. Transfer functions for measurement of velocity and temperature spectra by the Solent R3 sonic anemometer, $\theta = 0$.

by the transverse components, Equation (21), is less than the contamination of the transverse wind components by the streamwise component.

For the CSAT3, the attenuation of the vertical wind component at large k_* is considerably greater than for the horizontal wind components. One of the reasons for this is that the projection of the path lengths on the vertical, $\sqrt{3}\,p/2$, is greater than the horizontal projection, $p/2$ (Oncley, 1989). The disparity is significantly less for the Solents, where the vertical and horizontal projections are both $\sqrt{2}\,p/2$. As an additional consequence, the attenuation of the horizontal wind components is significantly less for the CSAT3 than for the Solent sonics.

The transfer functions for measurement of velocity spectra are also functions of wind direction θ with respect to the sonic paths. However, because of the symmetry of the arrays about the vertical axis, the transfer functions repeat themselves at wind direction intervals of 30°. The strongest dependence on wind direction occurs for the CSAT3 horizontal wind components and for the Solent streamwise wind component, all shown in Figure 5. The dependence of the remaining wind components on wind direction is negligible; see Tables BI and BII in Appendix B.

4. Spectral Transfer Functions for Sonic Temperature

The analysis is considerably simpler for sonic temperature because both it and its spectral density are scalars, rather than a vector and a tensor as for

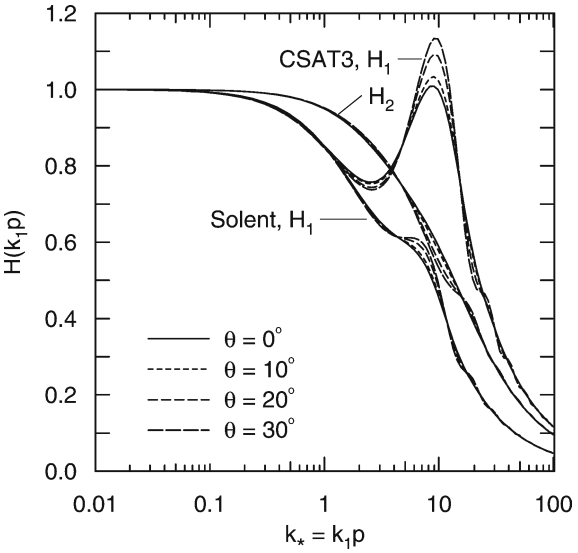

Figure 5. Transfer functions for measurement of selected horizontal wind component spectra as a function of wind direction, θ.

the wind velocity. The Solent R3 and the CSAT3 sonics average the speed of sound measured along all three paths (Table I),

$$H_{T_s}(k_1, \mathbf{p}) = \frac{\iint_{-\infty}^{\infty} \left(\frac{1}{3} \sum_{\alpha=a}^{c} \operatorname{sinc}(\mathbf{k} \cdot \mathbf{p}_\alpha) \right)^2 \Phi_{T_s}(\mathbf{k})\, dk_2\, dk_3}{\iint_{-\infty}^{\infty} \Phi_{T_s}(\mathbf{k})\, dk_2\, dk_3}. \tag{23}$$

The numerator of Equation (23) has been calculated numerically, as discussed previously. The transfer functions for CSAT3 and Solent R3 measurements of S_{T_s} are shown in Figures 3 and 4 and are tabulated in Appendix B. H_{T_s} for the two sonics is very similar and is less than those for the three velocity components. Their dependence on wind direction is negligible.

In contrast, the Solent R2 measures the speed of sound using only one of the three sonic paths, $\mathbf{p}_\alpha$, and thus

$$H_{T_s}(k_1, \mathbf{p}_\alpha) = \frac{\iint_{-\infty}^{\infty} \operatorname{sinc}^2(\mathbf{k} \cdot \mathbf{p}_\alpha)\, \Phi_{T_s}(\mathbf{k})\, dk_2\, dk_3}{\iint_{-\infty}^{\infty} \Phi_{T_s}(\mathbf{k})\, dk_2\, dk_3}. \tag{24}$$

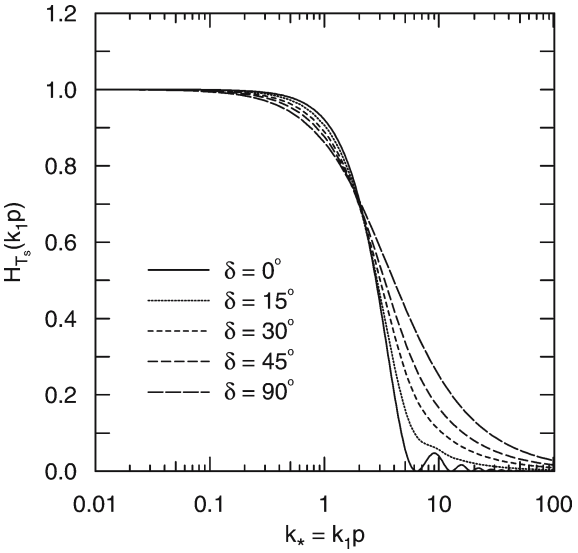

Figure 6. Transfer functions for measurement of sonic temperature spectra by a single sonic path.

For measurement of sonic temperature along a single path, Silverman (1968) provides an analytical result equivalent to Equation (8) for velocity,

$$H_{T_s}(k_1 p, \delta) = \frac{\Gamma(1/3)\, k_1^{5/3}}{3\sqrt{\pi}\,\Gamma(5/6)} \int_{-\infty}^{\infty} \frac{\operatorname{sinc}^2(k_1 p \cos\delta/2 + k' p \sin\delta/2)}{(k_1^2 + k'^2)^{4/3}}\, dk', \quad (25)$$

where our angle δ is the same as his θ. These transfer functions are shown in Figure 6 and have a dependence on δ similar to that for measurement of velocity along a single path, Figure 2. For the Solent R2, $\cos\delta \equiv \cos\phi\cos\theta$ with $\phi = 45°$, so that the range $0 \le \theta \le 90°$ corresponds to $45° \le \delta \le 90°$ in Figure 6, a range of δ for which H_{T_s} is less sensitive to wind direction. Note from comparison of Figures 6 and 4 that H_{T_s} for the Solent R3 is everywhere less than those for the Solent R2.

5. Concluding Discussion

The attenuation of inertial-range vertical velocity power spectra due to path averaging is found to be similar for the CSAT3 and Solent R2 and R3 sonics, when expressed as a function of $k_1 p$. The attenuation of the horizontal wind component spectra at large $k_1 p$ is significantly less than that of the vertical velocity spectra, more so for the CSAT3 than for the Solent sonics. The latter behaviour is attributed in part to the differences in the CSAT3 and Solent projected path lengths in the horizontal and

vertical directions. The transfer functions for measurements of the streamwise wind component spectra are found to have a local maximum in the range $5 \leq k_1 p \leq 10$, which is more pronounced for the CSAT3 sonic than for the Solents. With the exception of the CSAT3 measurement of the horizontal wind component spectra and the Solent measurement of the streamwise spectrum, the dependence of the transfer functions on wind direction is negligible. This is most likely a benefit of the symmetry of the path geometry about the vertical axis.

The sonic temperature spectrum is generally attenuated more than the wind component spectra, particularly when the measurement is averaged over all three paths. In the latter case, the attenuation is insensitive to wind direction and the differences between the CSAT3 and Solent R3 are negligible. The Solent R2 uses only one path for the measurement of the speed of sound and has less attenuation than the other two sonics, although it is still more than that of the horizontal wind component spectra and has a minor dependence on wind direction.

The dependence of sonic response on wavenumber is also an inverse function of path length, p, which is 0.1155 m for the CSAT3 and 0.15 m for the Solents. Figure 7 shows power spectral densities for velocity and temperature as fit to near-neutral observations by Kaimal et al. (1972), as a function of non-dimensional frequency fz/U where f is frequency, z is measurement height and U is mean wind speed. The spectral densities for velocity and temperature are normalized by velocity and temperature length scales, u_* and T_*, that are related to the vertical momentum and heat fluxes, respectively. Also shown are the spectral densities measured by a CSAT sonic anemometer after attenuation by path averaging. Figure 7a shows the case $z/p = 30$ where the attenuation is confined to the inertial subrange. Figure 7b shows the case $z/p = 5$ where the attenuation extends into the energy-containing range. In the latter case, Equations (4)–(5) for the spectral density tensor are no longer valid, and the expressions for attenuation derived here cannot be used to correct the measured spectra.

Measured power spectra are contaminated at high frequencies by several other instrumental errors not shown in Figure 7, including aliasing and possibly oversampling. KWH discuss in detail the correction of measured sonic anemometer power spectra for frequency-dependent errors and show that, for example,

$$S_3^m(f) = S_3(f)\, H_3(f) + \sum_{m=1}^{\infty} S_3(2mf_N - f)\, H_3(2mf_N - f) + \sum_{m=1}^{\infty} S_3(2mf_N + f)\, H_3(2mf_N + f) \tag{26}$$

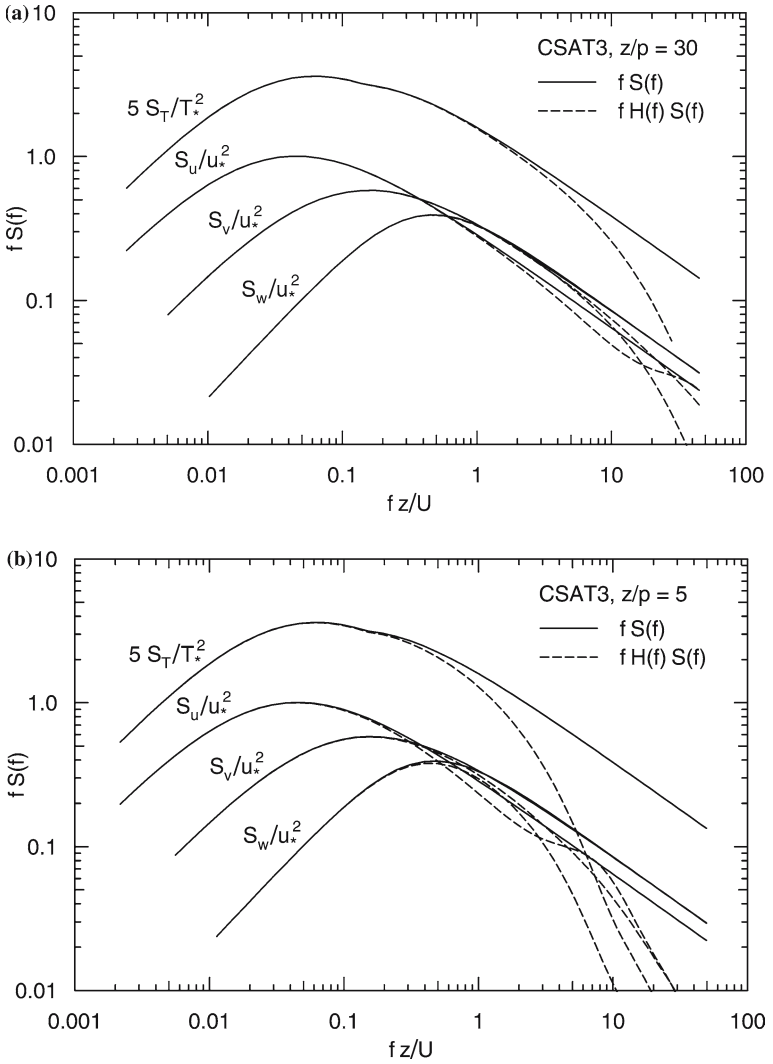

Figure 7. Spectral densities for velocity and temperature, $fS(f)$, and as attenuated by path–averaging, $fH(f)S(f)$, for a CSAT3 sonic with (a) $z/p=30$ and (b) $z/p=5$. See the text for definition of the velocity and length scales used for normalization.

$$= S_3(f) \sum_{m=-\infty}^{\infty} H_3(f_m)\,(f_m/f)^{-5/3}. \tag{27}$$

Here f_N is the Nyquist frequency, the sums account for aliasing, and $H_3(f) = H_3^p(f)H^a(f)$ accounts for attenuation of S_3 by sonic path averaging (H_3^p) and oversampling (H^a). Oversampling is discussed in Appendix C. Equation (27) assumes that f is in the inertial range and $f_m \equiv |f + 2mf_N|$.

Correction of the measured vertical velocity spectrum is then a simple matter of solving this equation for $S_3(f)$. An additional issue for correction of inertial–range power spectra is pulse sequence delay errors (Larsen et al., 1993), which we plan to discuss in a subsequent paper.

Note that the one-dimensional cospectral density for velocity is

$$Co_{ij}(k_1) = \iint_{-\infty}^{\infty} \Phi_{ij}(\mathbf{k})\, dk_2\, dk_2 = 0, \tag{28}$$

assuming the inertial-range spectral density tensor, Equation (4). Thus determination of cospectral attenuation due to path averaging requires a spectral density tensor for the energy–containing range, as proposed for scalar fluxes by Kristensen and Fitzjarrald (1984). Van Dijk (2002) extended their analysis to the CSAT3 and Solent sonics. Alternatively, the experimenter can choose the measurement height so that $k_1 p = 2\pi f p/U = 2\pi(fz/U)(p/z)$ is small enough to preclude attenuation by path averaging for the energy-containing eddies of the cospectrum.

Acknowledgements

The authors are grateful to Søren Larsen, Morten Nielson, Don Lenschow, and David Guararie for discussions of this research. The National Center for Atmospheric Research is funded by the National Science Foundation.

Appendix A: A Matrix Expression of C_{ij}

Oncley (1989) presented a matrix formulation of Equation (21), which we extend here to the case of an arbitrary alignment of the streamwise direction with respect to the sonic paths. We start by defining a matrix **A** to transform velocities parallel to the three sonic paths u_α, $\alpha = \{a, b, c\}$, to velocities in an orthogonal coordinate system aligned with the sonic, $\{u, v, w\}$, and a matrix **R** to rotate $\{u, v, w\}$ to velocities aligned with a streamwise coordinate system u_i, $i = \{1, 2, 3\}$. Thus

$$u_i = R_{ij} A_{j\alpha} u_\alpha. \tag{A1}$$

The summation convention applies to repeated subscripts in this and the following equations. Because of path averaging, the measured wind components cannot be computed from the inverse of this equation. Instead, these measurements are given by

$$u_\alpha^m = A_{\alpha i}^{-1} R_{ij}^{-1} \tilde{u}_j^\alpha, \tag{A2}$$

where $\mathbf{A}^{-1}$ and $\mathbf{R}^{-1}$ are the inverses of matrices $\mathbf{A}$ and $\mathbf{R}$, and $\tilde{u}_j^{\alpha}$ is defined by Equation (15). Finally, combining the preceding Equations with Equations (16, 17, and 19) gives

$$C_{ij} = R_{ik} A_{k\alpha} A_{\alpha l}^{-1} R_{lj}^{-1} \operatorname{sinc}(\mathbf{k} \cdot \mathbf{p}_{\alpha}/2). \tag{A3}$$

Note that the sinc function depends on $\mathbf{p}_{\alpha}$ and must be included when summing over the corresponding subscripts of the transformation matrices $\mathbf{A}$ and $\mathbf{A}^{-1}$. Without the sinc function dependence on α, C_{ij} defined by Equation (A3) would be equal to the identity matrix δ_{ij}.

For the the generic UW sonic geometry discussed here

$$\mathbf{A} = \frac{2}{3\cos\phi} \begin{bmatrix} -1 & \cos(\pi/3) & \cos(\pi/3) \\ 0 & \sin(\pi/3) & -\sin(\pi/3) \\ 1/(2\tan\phi) & 1/(2\tan\phi) & 1/(2\tan\phi) \end{bmatrix}, \tag{A4}$$

and

$$\mathbf{A}^{-1} = \cos\phi \begin{bmatrix} -1 & 0 & \tan\phi \\ \cos(\pi/3) & \sin(\pi/3) & \tan\phi \\ \cos(\pi/3) & -\sin(\pi/3) & \tan\phi \end{bmatrix}. \tag{A5}$$

For the simple coordinate rotation of Equation (11),

$$\mathbf{R} = \begin{bmatrix} \cos\theta & \sin\theta & 0 \\ -\sin\theta & \cos\theta & 0 \\ 0 & 0 & 1 \end{bmatrix} \tag{A6}$$

and, since $\mathbf{R}$ is orthogonal, the inverse of $\mathbf{R}$ is equal to its transpose, $\mathbf{R}^{-1} = \mathbf{R}^{\mathrm{T}}$. For the more complex coordinate rotation matrix required to correct for sonic tilt, see for example Wilczak et al. (2001).

Appendix B: Computed Transfer Functions (Tables BI–BIII)

Appendix C: Oversampling

The data series that is output by current sonic anemometers is commonly either every measurement sample or data values that are averages over n samples, where 'sample' denotes the wind and temperature values computed from a single set of six pulses (two pulses in opposite directions for each of the three paths). The latter process is called oversampling. The major benefit of oversampling is to decrease the noise in the output data by $n^{-1/2}$.

TABLE BI

CSAT3 transfer functions for velocity power spectra.

	$H_1(k_1 p)$				$H_2(k_1 p)$				$H_3(k_1 p)$			
$k_1 p$	$\theta = 0°$	10°	20°	30°	$\theta = 0°$	10°	20°	30°	$\theta = 0°$	10°	20°	30°
0.0100	1.000	1.000	1.000	1.000	1.000	1.000	1.000	1.000	1.000	1.000	1.000	1.000
0.0158	0.999	0.999	0.999	0.999	1.000	1.000	1.000	1.000	1.000	1.000	1.000	1.000
0.0251	0.999	0.999	0.999	0.999	1.000	1.000	1.000	1.000	1.000	1.000	1.000	1.000
0.0398	0.998	0.998	0.998	0.998	0.999	0.999	0.999	0.999	0.999	0.999	0.999	0.999
0.0631	0.996	0.996	0.996	0.996	0.999	0.999	0.999	0.999	0.999	0.999	0.999	0.999
0.100	0.992	0.992	0.992	0.992	0.998	0.998	0.998	0.998	0.998	0.998	0.998	0.998
0.158	0.984	0.984	0.984	0.984	0.996	0.996	0.996	0.996	0.995	0.995	0.995	0.995
0.251	0.970	0.970	0.970	0.970	0.993	0.993	0.993	0.993	0.990	0.990	0.990	0.990
0.398	0.946	0.946	0.945	0.945	0.986	0.986	0.986	0.986	0.980	0.980	0.980	0.980
0.631	0.906	0.906	0.905	0.904	0.972	0.973	0.973	0.974	0.959	0.959	0.959	0.959
1.00	0.851	0.850	0.847	0.846	0.949	0.949	0.951	0.951	0.920	0.920	0.920	0.920
1.58	0.790	0.787	0.782	0.779	0.910	0.911	0.914	0.915	0.849	0.849	0.849	0.850
2.51	0.757	0.753	0.744	0.738	0.852	0.854	0.859	0.861	0.729	0.730	0.730	0.730
3.98	0.807	0.804	0.798	0.794	0.778	0.779	0.782	0.784	0.554	0.554	0.554	0.554
6.31	0.950	0.959	0.983	0.999	0.691	0.685	0.674	0.668	0.347	0.347	0.346	0.345
10.0	0.992	1.018	1.080	1.125	0.583	0.571	0.545	0.528	0.180	0.179	0.175	0.173
15.8	0.717	0.715	0.704	0.687	0.452	0.451	0.451	0.455	0.102	0.102	0.104	0.105
25.1	0.443	0.442	0.445	0.462	0.323	0.324	0.324	0.321	0.0646	0.0645	0.0640	0.0626
39.8	0.284	0.283	0.283	0.292	0.219	0.219	0.220	0.218	0.0398	0.0398	0.0398	0.0391
63.1	0.180	0.180	0.180	0.174	0.144	0.144	0.145	0.146	0.0248	0.0248	0.0248	0.0253
100	0.114	0.114	0.114	0.116	0.0933	0.0934	0.0934	0.0937	0.0155	0.0155	0.0155	0.0154

TABLE BII

Solent R2 and R3 transfer functions for velocity power spectra.

	$H_1(k_1 p)$				$H_2(k_1 p)$				$H_3(k_1 p)$			
$k_1 p$	$\theta = 0°$	10°	20°	30°	$\theta = 0°$	10°	20°	30°	$\theta = 0°$	10°	20°	30°
0.0100	1.000	1.000	1.000	1.000	1.000	1.000	1.000	1.000	1.000	1.000	1.000	1.000
0.0158	1.000	1.000	1.000	1.000	1.000	1.000	1.000	1.000	1.000	1.000	1.000	1.000
0.0251	0.999	0.999	0.999	0.999	1.000	1.000	1.000	1.000	1.000	1.000	1.000	1.000
0.0398	0.998	0.998	0.998	0.998	0.999	0.999	0.999	0.999	0.999	0.999	0.999	0.999
0.0631	0.997	0.997	0.997	0.997	0.999	0.999	0.999	0.999	0.999	0.999	0.999	0.999
0.100	0.993	0.993	0.993	0.993	0.998	0.998	0.998	0.998	0.998	0.998	0.998	0.998
0.158	0.986	0.986	0.986	0.986	0.996	0.996	0.996	0.996	0.996	0.996	0.996	0.996
0.251	0.974	0.974	0.974	0.974	0.991	0.991	0.991	0.991	0.991	0.991	0.991	0.991
0.398	0.951	0.951	0.951	0.950	0.982	0.982	0.982	0.982	0.982	0.982	0.982	0.982
0.631	0.911	0.911	0.911	0.911	0.965	0.965	0.965	0.965	0.963	0.963	0.963	0.963
1.00	0.850	0.850	0.849	0.848	0.933	0.933	0.933	0.934	0.926	0.926	0.926	0.926
1.58	0.768	0.767	0.765	0.763	0.875	0.875	0.877	0.878	0.857	0.857	0.857	0.858
2.51	0.683	0.680	0.675	0.673	0.781	0.782	0.785	0.786	0.736	0.736	0.737	0.737
3.98	0.621	0.620	0.618	0.617	0.650	0.650	0.651	0.652	0.550	0.550	0.551	0.552
6.31	0.573	0.580	0.598	0.609	0.502	0.498	0.491	0.486	0.337	0.336	0.334	0.333
10.0	0.448	0.454	0.468	0.477	0.365	0.362	0.355	0.352	0.192	0.192	0.190	0.189
15.8	0.280	0.277	0.271	0.267	0.252	0.253	0.255	0.256	0.126	0.126	0.128	0.129
25.1	0.179	0.179	0.178	0.173	0.168	0.168	0.168	0.170	0.0795	0.0795	0.0801	0.0814
39.8	0.114	0.114	0.115	0.117	0.110	0.109	0.109	0.109	0.0503	0.0503	0.0503	0.0497
63.1	0.0724	0.0725	0.0726	0.0729	0.0705	0.0705	0.0704	0.0706	0.0318	0.0318	0.0318	0.0319
100	0.0458	0.0459	0.0460	0.0462	0.0451	0.0450	0.0450	0.0456	0.0201	0.0201	0.0201	0.0202

TABLE BIII

Transfer functions for temperature power spectra, $H_{T_S}(k_1 p)$.

	CSAT3				Solent R3				Solent R2			
$k_1 p$	$\theta = 0°$	10°	20°	30°	$\theta = 0°$	10°	20°	30°	$\theta = 0°$	30°	60°	90°
0.0100	1.000	1.000	1.000	1.000	1.000	1.000	1.000	1.000	1.000	1.000	1.000	1.000
0.0158	1.000	1.000	1.000	1.000	1.000	1.000	1.000	1.000	1.000	1.000	1.000	1.000
0.0251	0.999	0.999	0.999	0.999	0.999	0.999	0.999	0.999	1.000	0.999	0.999	0.999
0.0398	0.999	0.999	0.999	0.999	0.999	0.999	0.999	0.999	0.999	0.999	0.999	0.999
0.0631	0.997	0.997	0.997	0.997	0.997	0.997	0.997	0.997	0.998	0.998	0.997	0.997
0.100	0.994	0.994	0.995	0.995	0.995	0.995	0.995	0.995	0.996	0.996	0.995	0.994
0.158	0.989	0.989	0.989	0.989	0.990	0.990	0.990	0.990	0.992	0.991	0.989	0.989
0.251	0.978	0.978	0.978	0.978	0.980	0.980	0.980	0.980	0.984	0.982	0.979	0.978
0.398	0.958	0.958	0.958	0.958	0.960	0.960	0.960	0.960	0.967	0.964	0.959	0.957
0.631	0.921	0.921	0.921	0.921	0.923	0.923	0.923	0.923	0.935	0.931	0.924	0.921
1.00	0.856	0.856	0.856	0.856	0.857	0.857	0.857	0.857	0.875	0.870	0.863	0.860
1.58	0.753	0.753	0.753	0.753	0.747	0.747	0.747	0.748	0.770	0.769	0.768	0.768
2.51	0.604	0.605	0.605	0.605	0.582	0.582	0.583	0.583	0.613	0.621	0.636	0.643
3.98	0.422	0.422	0.422	0.422	0.377	0.377	0.376	0.375	0.425	0.447	0.484	0.500
6.31	0.242	0.241	0.240	0.239	0.189	0.188	0.184	0.181	0.264	0.293	0.341	0.361
10.0	0.115	0.113	0.111	0.108	0.0879	0.0877	0.0873	0.0874	0.163	0.186	0.228	0.247
15.8	0.0615	0.0619	0.0633	0.0649	0.0541	0.0546	0.0557	0.0559	0.101	0.118	0.149	0.164
25.1	0.0378	0.0378	0.0373	0.0361	0.0321	0.0322	0.0327	0.0337	0.0635	0.0750	0.0963	0.106
39.8	0.0227	0.0228	0.0227	0.0221	0.0196	0.0196	0.0196	0.0191	0.0399	0.0474	0.0616	0.0683
63.1	0.0139	0.0139	0.0140	0.0143	0.0121	0.0121	0.0121	0.0122	0.0251	0.0300	0.0392	0.0436
100	0.00863	0.00864	0.00864	0.00854	0.00751	0.00752	0.00752	0.00747	0.0158	0.0189	0.0249	0.0277

The Fourier transform for averaging over n samples is

$$\begin{aligned} dZ_a(f) &= \frac{e^{-i\omega(n-1)t_s/2}}{n} \sum_{k=0}^{n-1} e^{i\omega k t_s} \\ &= \frac{e^{-i\omega(n-1)t_s/2}}{n} \frac{[1-e^{i\omega n t_s}]}{[1-e^{i\omega t_s}]} \\ &= \frac{2\sin(\omega t_s/2)\,\sin(\omega n t_s/2)}{n[1-\cos(\omega t_s)]} \end{aligned} \tag{C1}$$

where $\omega = 2\pi f$ and t_s is the time interval between data samples, e.g. 16.7 ms for a CSAT3 sonic sampling at 60 Hz. Figure C1 shows the transfer function $H^a \equiv dZ_a dZ_a^*$ for an average of three samples, as might be used to obtain a 20 Hz output from a CSAT3.

The first zero of the transfer function occurs at $f = 1/nt_s$, the sample rate of the oversampled data. For $\omega t_s \ll 1$ or $n \gg 1$, $H^a(ft_s \leq 0.5)$ approaches $\mathrm{sinc}^2(\omega n t_s/2)$, the transfer function for a continuous block average of width nt_s. In these limits, the amplitude of H^a at the Nyquist frequency of the oversampled data, $f_N = 1/2nt_s$, is $(2/\pi)^2 = 0.405$. At frequencies greater than $1/2t_s$ (the Nyquist frequency of the sample rate), H^a is no longer approximated by $\mathrm{sinc}^2(\omega n t_s/2)$. For $f > 1/2t_s$, $H^a(0.5 < ft_s \leq 1)$ is the mirror image of its values at lower frequencies, and then $H^a(ft_s > 1)$ repeats itself periodically at frequency intervals of $1/t_s$.

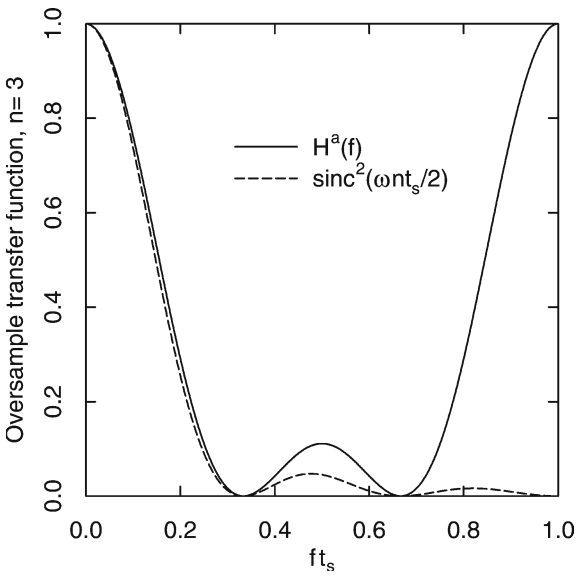

Figure C1. Transfer function for oversampling by $n = 3$ samples, as a function of ft_s.

Henjes et al. (1999) previously presented an analysis of oversampling similar to Equation (C1). Our analysis differs from theirs by a phase angle equal to $\omega(n-1)t_s/2$, because we assume that the averaged sample represents the measured variable at a time equal to the mid-point of the averaging period rather than the start of the averaging period. This phase factor permits a simple expression for the Fourier transform, Equation (C3), and drops out when calculating the transfer function.

References

Fairall, C. W., Bradley, E. F., Hare, J. E., Grachev, A. A., and Edson, J. B.: 2003, 'Bulk Parameterization of Air-sea fluxes: Updates and Verification for the COARE Algorithm', *J. Climate* **16**, 571–591.

Henjes, K., Taylor, P. K., and Yelland, M. J.: 1999, 'Effect of Pulse Averaging on Sonic Anemometer Spectra', *J. Atmos. Oceanic Tech.* **16**, 181–184.

Horst, T. W., 1973, 'Spectral Transfer Functions for a Three-component Sonic Anemometer', *J. Appl. Meteorol.* **12**, 1072–1075.

Howell, J. F., and Sun, J.: 1999, 'Surface-layer Fluxes in Stable Conditions', *Boundary-Layer Meteorol.* **90**, 495–520.

Kaimal, J. C., Wyngaard, J. C., and Haugen, D. A.: 1968, 'Deriving Power Spectra from a Three-component Sonic Anemometer', *J. Appl. Meteorol.* **7**, 827–837.

Kaimal, J. C., Wyngaard, J. C., Izumi, Y., and Cote, O. R.: 1972, 'Spectral Characteristics of Surface-layer Turbulence', *Quart. J. Roy. Meteorol. Soc.* **98**, 563–589.

Kristensen, L. and Fitzjarrald, D. R.: 1984, 'The Effect of Line Averaging on Scalar Flux Measurements With a Sonic Anemometer near the Surface', *J. Atmos. Oceanic Tech.* **1**, 138–146.

Larsen, S. E., Edson, J. B. Fairall, C. W., and Mestayer, P. G.: 1993, 'Measurement of Temperature Spectra by a Sonic Anemometer', *J. Atmos. Oceanic Tech.* **10**, 345–354.

Mahrt, L., Vickers, D., Nakamura, R., Soler, M. R., Sun, J., Burns, S., and Lenschow, D. H.: 2001, Shallow Drainage Flows', *Boundary-Layer Meteorol.* **101**, 243–260.

Oncley, S. P.: 1989, *Flux Parameterization Techniques in the Atmospheric Surface Layer*. Ph.D. Dissertation, University of California, Irvine CA, 202 pp.

Pope, S. B.: 2000, *Turbulent Flows*, Cambridge University Press, U.K., 771 pp.

Press, W. H., Teukolsky, S. A., Vetterling, W. T., and Flannery, B. P.: 1992, *Numerical Recipes, 2nd edn.*, Cambridge University Press, U.K., 963 pp.

Silverman, B. A.: 1968, 'The Effect of Spatial Averaging on Spectrum Estimation', *J. Appl. Meteorol.* **7**, 168–172.

Tennekes, H. and Lumley, J. L.: 1972, *A First Course in Turbulence*, The MIT Press, Boston, 300 pp.

van Dijk, A.: 2002, 'Extension to 3D of "The Effect of Line Averaging on Scalar Flux measurements with a Sonic Anemometer near by surface" by Kristensen and Fitzjarrald', *J. Atmos. Oceanic Tech.* **19**, 80–82.

Wilczak, J. M., Oncley, S. P., and Stage, S. A.: 2001, 'Sonic Anemometer Tilt Correction Algorithms. *Boundary-Layer Meteorol.*, **99**, 127–150.

Wyngaard, J. C. and Zhang, S. F. 1985, 'Transducer Shadow Effects on Turbulence Spectra Measured by Sonic Anemometers', *J. Atmos. Oceanic Tech.* **2**, 548–558.

Zhang, S. F., Wyngaard, J. C., Businger, J. A., and Oncley, S. P.: 1986, 'Response Characteristics of the U. W. Sonic Anemometer', *J. Atmos. Oceanic Tech.* **3**, 315–323.